Unified Framework for Stability Analysis and Controller Design for Multi-Converter MVDC Grids

Navid Rahbariasr[1], W. Wesley Pennington[2], Matthias Preindl[1]
[1] *Department of Electrical Engineering, Columbia University*, New York, USA
[2] *Tau Motors, Inc.*, Redwood City, USA
nr3051@columbia.edu, wesley@taumotors.com, matthias.preindl@columbia.edu

***Abstract*—This paper presents a novel unified framework for the stability analysis of multi-converter systems in Medium-Voltage Direct Current (MVDC) grids. The proposed framework integrates the effect of line dynamics, controller dynamics, sampling-time, filter capacitance, and grid-forming/grid-following mode of the converter into a single analytical formulation. Therefore, it enables a detailed study of the interactions among a variety of distinct but interconnected parameters and their effects on the small-signal stability of the system through stability maps. This holistic perspective facilitates the identification of control strategies that ensure robust stability in a broad range of operating conditions. The effectiveness of the approach is demonstrated through various time-domain simulations.**

***Index Terms*—MVDC grids, multi-converter stability, grid-forming converters, grid-following converters, droop control, controller design**

I. Introduction

Medium-voltage direct current (MVDC) networks are arising as a promising architecture for future electric power distribution systems [1]. Compared to conventional AC grids, MVDC networks offer higher efficiency and improved reliability over multiple applications [2] and facilitate easier integration of distributed energy resources and storage devices. However, the stable operation of the MVDC grids, in a converter dominated scenario is challenging due to the strong coupling among multiple converters, the influence of controller parameters, and the dynamics of the network interconnections.

Stability of DC networks has received attention in recent years. Su et al. [3] has analyzed multi-converter DC microgrids under Constant Power Loads (CPL) and has derived some sufficient conditions for stability but has only considered single-bus architectures and neglected controller dynamics. Huangfu et al. [4] and Pang et al. [5] have investigated stabilization methods for DC grids focusing on input filters and nonlinear control but only at the single converter level without addressing multi-converter interactions. Anand and Fernandes [6] considered multi-bus DC networks with reduced-order models under multi-bus structures, but converter controller dynamics were not explicitly included. Navarro-Rodríguez et al. [7] and Gui et al. [8] have studied converter-level stability though their scope remained restricted to single-converter systems.

In LVDC networks, stability analysis often assumes ideal or resistive interconnections. Therefore, studies that have analyzed the transient stability problems in DC systems such as Decun et al. [9] have often neglected the effect of line inductance. In contrast, one important factor that differentiates MVDC microgrids from low-voltage DC (LVDC) systems is that they enable medium-distance distribution and interconnection of multiple feeders, energy sources, and loads. As a result, the line impedance, particularly the inductive components, are no longer negligible. The interaction between converter dynamics and line dynamics can significantly influence stability and neglecting these effects may lead to inaccurate predictions.

Analyzing the stability of MVDC systems requires a more comprehensive framework that can capture multi-converter interactions, controller dynamics, and network line dynamics in a multi-bus structure simultaneously. Furthermore, most prior analyses rely on continuous-time approximations and do not incorporate the effects of discrete-time controller implementation and sampling, which also play a critical role in the transient interactions as we show in this paper.

To address this gap, this paper provides a unified and comprehensive framework, that explicitly includes line dynamics in combination with converter control loops and sampling effects in a multi-bus structure for MVDC grid stability analysis. The framework integrates discrete-time converter control models with network dynamics, and explicitly accounts for sampling effects. It enables eigenvalue-based stability assessment through the construction of stability maps. By doing so, it provides a systematic tool to guide the selection of controller gains, droop coefficients, mode allocations (grid-forming vs. grid-following), and sampling frequencies that ensure robust operation under diverse operating conditions.

The rest of this paper is organized as follows: Section II describes modeling assumptions and presents the proposed framework. Section III provides the simulation results to validate the framework predictions and showcase its application. Section IV concludes the paper with a summary and directions for future work.

II. Proposed Framework

A. Converter Models and Control Dynamics

As shown in Fig 1, each converter is abstracted as a controlled current source, which provides a level of detail sufficient to capture network transients while avoiding the complexity of switching-level dynamics. Both grid-forming (GFM) and grid-following (GFL) controllers are modeled: **Grid-forming converter:** Implements a voltage regulation

979-8-3315-8138-1

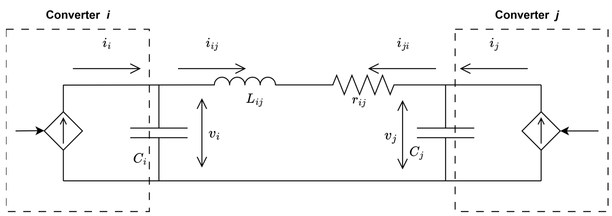

Fig. 1. Abstracting each converter as a controlled current source.

loop with proportional–integral (PI) control. The current injection at the i-th converter is updated as follows:

$$i_i[k+1] = i_i[k] + K_p(v_i^{\text{ref}} - v_i[k]) + K_i z_i[k], \quad (1)$$

$$z_i[k+1] = z_i[k] + T_s(v_i^{\text{ref}} - v_i[k]), \quad (2)$$

where K_p and K_i are PI controller gains, T_s is the sampling time, $z_i[k]$ is the integrator state, and v_i^{ref} and $v_i[k]$ are the reference voltage and the measured voltage of the converter output respectively. The goal of the grid-forming converter is to regulate the voltage of the bus. v_i^{ref} is calculated as follows:

$$v_i^{\text{ref}} = v_i^* - r_i^d i_i[k] \quad (3)$$

where r_i^d is the droop coefficient for converter i, and v_i^* is the set-point value for voltage that is sent to the converter via an energy management system.

Grid-following converter: Operates with power regulation. The current reference is computed as:

$$i_i[k+1] = \frac{P_i^{\text{ref}}}{v_i[k]}, \quad (4)$$

where P_i^{ref} is the active power reference. The goal of the grid-following converter is to follow the reference power provided by an energy management system for the micro grid.

B. Network Representation and Line Dynamics

The physical dynamics of the DC network are represented by capacitor and inductor differential equations:

$$C_i \frac{dv_i}{dt} = i_i - \sum_j i_{ij}, \quad (5)$$

$$L_{ij} \frac{di_{ij}}{dt} = v_i - v_j - r_{ij} i_{ij}, \quad (6)$$

where C_i is the capacitance of the converter terminal, L_{ij} and r_{ij} are the line inductance and resistance between converters i and j, and i_{ij} is the line current passing from node i to j.

C. Discretization and Closed-loop Dynamics

The converter controllers are inherently implemented in discrete time with sampling period T_s, while the physical network dynamics evolve in continuous time. To consistently analyze the system, the network dynamics are discretized with step size T_s and then integrated with the discrete-time control laws. The plant dynamics are linear and their state-space representation can be as follows:

$$\dot{\mathbf{x}}_p(t) = A_p \mathbf{x}_p(t) + B_p \mathbf{u}_p(t), \quad (7)$$

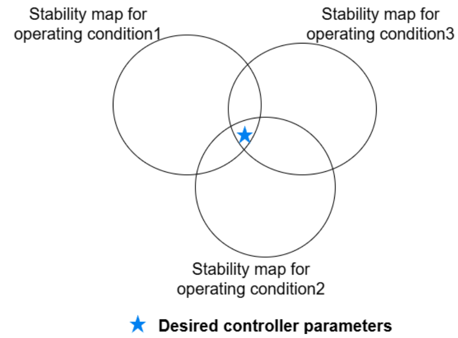

Fig. 2. Choosing control parameters based on overlap of stability maps.

where $\mathbf{x}_p(t)$ is a vector representing the plant states (node voltages and line currents), $\mathbf{u}_p(t)$ is the vector of converter injected currents, and the matrices A_p and B_p represent the state and input matrices respectively. Discretization with sampling period T_s gives

$$\mathbf{x}_p[k+1] = A_{pd}\mathbf{x}_p[k] + B_{pd}\mathbf{u}_p[k], \quad (8)$$

with $A_{pd} = e^{A_p T_s}$ and $B_{pd} = \int_0^{T_s} e^{A_p \tau} B_p \, d\tau$. On the controller side, it is important to note that the system is not strictly linear. In particular, the grid-following (GFL) converter introduces nonlinearities through its current control rule eq. (4). Linearizing this control rule around a certain operating point returns the following:

$$\Delta i_i[k+1] = \frac{-P_i^{\text{ref}}}{(v_i^*)^2} \Delta v_i[k], \quad (9)$$

which depends inversely on the square of the bus voltage. The discrete-time converter controllers can then be expressed as

$$\mathbf{x}_c[k+1] = A_c\mathbf{x}_c[k] + B_c\mathbf{y}_p[k], \quad \mathbf{u}_p[k] = C_c\mathbf{x}_c[k] + D_c\mathbf{y}_p[k], \quad (10)$$

where $\mathbf{x}_c[k]$ is the vector of the controllers states, i.e. integrator states, and $\mathbf{y}_p[k]$ is a subset of the plant states, i.e. converter output voltage and current measurements used by the controllers.

By substituting $\mathbf{u}_p[k]$ into the discretized plant equation and recognizing that $\mathbf{y}_p[k] \subset \mathbf{x}_p[k]$, the closed-loop dynamics can be written compactly as

$$\begin{bmatrix} \mathbf{x}_p[k+1] \\ \mathbf{x}_c[k+1] \end{bmatrix} = \underbrace{\begin{bmatrix} A_{pd} + B_{pd}D_c\Gamma & B_{pd}C_c \\ B_c\Gamma & A_c \end{bmatrix}}_{A_{\text{cl}}} \begin{bmatrix} \mathbf{x}_p[k] \\ \mathbf{x}_c[k] \end{bmatrix}, \quad (11)$$

where Γ is a selection matrix that extracts the relevant plant states (converter output voltage and current) for controller feedback. The resulting closed-loop system in (11) is autonomous, since the interconnection of plant and controller eliminates explicit inputs.

D. Stability Assessment

Small-signal stability of the closed-loop multi-converter system is assessed using the spectral radius of the closed-loop system matrix A_{cl} in (11), where stability is ensured if

979-8-3315-8138-1

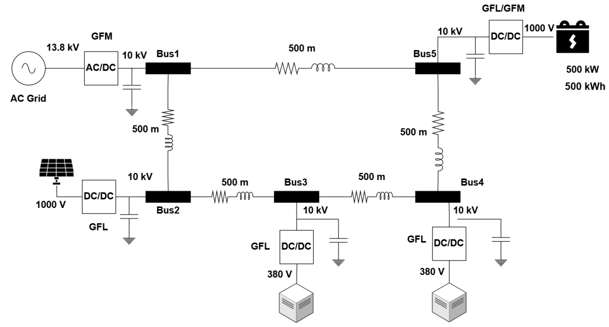

Fig. 3. Architecture of the five-converter DC test system. GFM and GFL converters are interconnected through R–L lines.

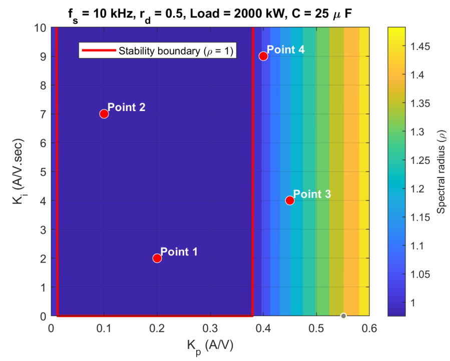

Fig. 4. Stability map of the five-converter system in terms of K_p and K_i of a GFM converter. The region inside the red boundary indicates stable combinations. Markers denote parameter sets selected for time-domain simulation.

$\rho(A_{\text{cl}}) < 1$. The spectral radius $\rho(\cdot)$ denotes the maximum magnitude of the eigenvalues of a matrix. For a fixed network configuration, sampling time T_s, converter mode allocation, pre-allocated droop gains r_d, and homogeneous GFM converters, stability maps are constructed in the (K_p, K_i) plane for different operating points. Robust controller gains are selected from the overlap of these stability maps, as illustrated in Fig. 2, using the following procedure:

1: Specify operating points $\{\mathcal{O}_i\}$.
2: **for** each $\mathcal{O}_i$ **do**
3: Compute $\mathcal{S}_i = \{(K_p, K_i) : \rho(A_{\text{cl}}(K_p, K_i; \mathcal{O}_i)) < 1\}$.
4: **end for**
5: Select $(K_p, K_i) \in \bigcap_i \mathcal{S}_i$.

III. Simulation Studies

A. Simulation Setup

To validate the proposed framework, a five-converter 10 kV DC network is considered as shown in Fig. 3. Each converter is connected to a local bus through a filter capacitor, and buses are interconnected by resistive-inductive lines. The converter connected to AC grid is always in GFM mode, the converter connected to the storage device can be in GFM or GFL mode and the remaining converters are in GFL modes. The nominal parameters for the lines considering the 500 m length are calculated as: $L = 250$ μH, and $R_{\text{line}} = 0.2$ Ω. The converters are modeled as controllable current sources in alignment with the assumptions of the proposed framework. The physical layer is implemented in PLECs v4.9.4, while the control layer is implemented in Simulink in MATLAB R2024b.

B. Case Studies

Validation of Framework Predictions: The first case evaluates whether the stability regions predicted by the framework match time-domain simulations. The system configuration consists of two data center loads of 1 MW each, supplied by an AC source (1 MW), a PV source (500 kW), and a battery (500 kW). The controller sampling frequency is set to 10 kHz, the droop coefficient to $r_d = 0.5$, and the filter capacitance to 25 μF. Fig. 4 shows a stability map in terms of the proportional and integral gains (K_p, K_i) of the AC/DC converter operating in GFM mode. The stability map is generated by sweeping across a range of K_p, K_i values and identifying the parameter combinations where the eigenvalues of A_{cl} (as in (11)) are all inside the unit circle. Parameter combinations located inside the red region correspond to stable combinations. Four representative points are selected inside and outside the predicted stability region, and time-domain simulations are conducted to evaluate the dynamic response. As the generation and load are initially unbalanced at each bus, the capacitor voltages redistribute dynamically to cause current flows across buses, and let power flow from buses that generate power to the buses that need power. This creates transient interactions between network and controller dynamics, which could converge to a steady state (stable) or diverge (unstable).

Fig. 5 shows the simulation results for the four tested operating points. Consistent with the stability map predictions, parameter combinations 1 and 2 result in stable trajectories, while combinations 3 and 4 lead to instability. To further validate the proposed framework, small-disturbance tests were conducted. Fig. 6 shows the simulation results, for controller parameter chosen as per Points 1, subject to a 1% perturbation in reference voltage and load at $t = 1$ s. The results demonstrate that, following these disturbances, the voltages stably converge to new operating points in agreement with the framework prediction.

Effect of Controller Sampling Time: The role of sampling time T_s is next investigated. Note that controller frequency is defined as $f_s = 1/T_s$. Fig. 7 shows the stability region for sampling frequencies of 20 kHz and 5 kHz with the same points marked in Fig. 4. It can be seen that a higher sampling frequency enlarges the stability region, while a lower frequency shrinks it. As a result, points 3 and 4 that were unstable with 10 kHz become stable at 20 kHz, and point 1 that was stable with 10 kHz sampling becomes unstable with 5 kHz sampling.

Effect of Droop Coefficients: Fig. 8 shows the stability regions for droop coefficients of 0.1 and 1 with the same points marked in Fig. 4. It shows that higher droop coefficient results in a larger stability region for the system. However, a larger droop coefficient means a larger deviation from the reference voltage

979-8-3315-8138-1

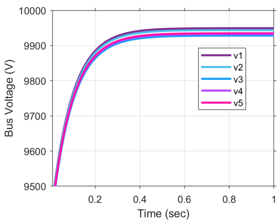

(a) Parameters 1 (stable).

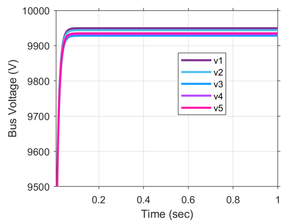

(b) Parameters 2 (stable).

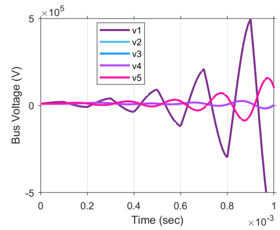

(c) Parameters 3 (unstable).

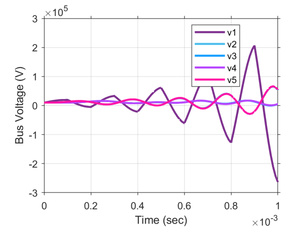

(d) Parameters 4 (unstable).

Fig. 5. Time-domain simulation results for four parameter combinations from Fig. 4. Subfigures (a)–(d) correspond to operating points 1–4, respectively. Stable responses are observed in (a) and (b), while instability occurs in (c) and (d).

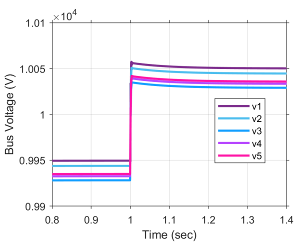

(a) Voltage reference perturbation

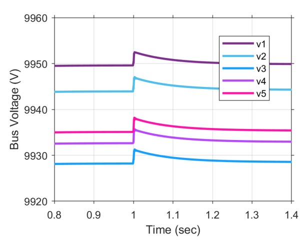

(b) Load perturbation

Fig. 6. Small-disturbance tests for controller parameters selected at Point 1. The figures illustrate the voltage response under (a) a 1% change in voltage reference and (b) a 1% change in load value.

per (3).

Effect of Filter Capacitance: The impact of terminal capacitance C is also assessed. Fig. 9 shows the stability region for filter capacitance values of 15 μF and 20 μF. It shows that the stability region is shrinking rapidly with decrease in capacitance value, such that when using 15 μF the system is unstable for all marked four points. Fig. 10 shows the stability maps for the same capacitance values with increased sampling frequency of 20 kHz. It can be seen that increasing the sampling frequency has made the stability region larger for smaller capacitance values. These results indicate stability can be preserved even with smaller capacitance values. However, the relationship is not monotonic. Fig. 11 shows the stability region in terms of capacitance and sampling frequency when the load is 20 MW revealing regions where increasing the frequency or capacitance does not guarantee stability. This behavior results from dynamic coupling between discrete-time controller and network modes. Fig. 12 shows the trajectory of some of the system modes as frequency varies for the

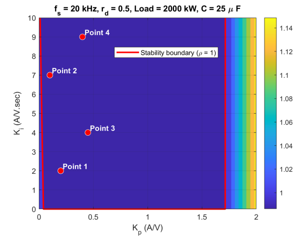

(a) 20 kHz sampling frequency

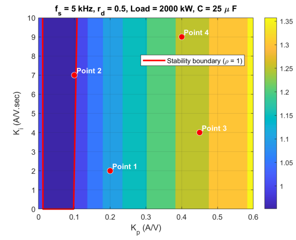

(b) 5 kHz sampling frequency

Fig. 7. Higher controller sampling frequency enlarges the stable region, while lower frequency shrinks it.

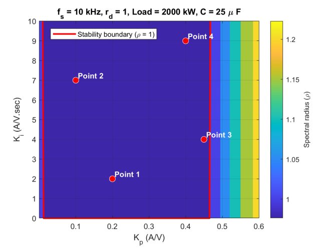

(a) r_d=1

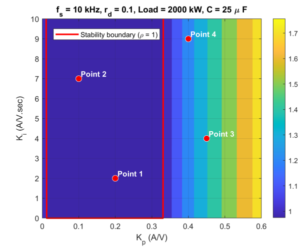

(b) r_d=0.1

Fig. 8. Effect of droop coefficient on stability region. Higher droop enlarges the stable region, while lower droop shrinks it.

same operating condition. As sampling frequency changes, the discrete-time plant representation in (8) changes, modifying how each mode interacts with the controller. Some modes become more damped while others become less damped and exit the unit circle. The effect is amplified at high CPL penetration due to reduced damping margins.

Effect of Load Variation: The influence of increasing load demand on stability is examined. Fig. 13 shows the stability maps when the load is increased to 10 MW and 30 MW. It is seen that as load increases, the stability region shrinks. However, as seen in the figures, the regions have overlap with each other. For instance, Point 1, is in the stable region regardless of the load demand. This means that choosing the value of K_p, and K_i, as Point 1, ensures the system is stable under different load conditions. Fig. 14 shows the simulation results in time-domain, when the load of the system increases from 2 MW to 5 MW at 1 s intervals. It can be seen that despite sudden changes in the load (which is typical of data centers), the controllers are able to stabilize the voltage, and steer the system toward the new operating point.

IV. Conclusion

This paper presented a unified framework for stability analysis and controller design of multi-converter MVDC grids. The framework explicitly incorporates line dynamics, converter control loops, and sampling effects and integrates them with discrete-time controller models. Future research will focus on validating the framework on hardware setups.

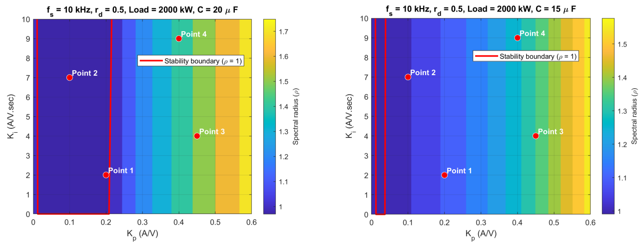

(a) $C = 20\mu F, f_s = 10kHz$ (b) $C = 15\mu F, f_s = 10kHz$

Fig. 9. Effect of terminal capacitance C on stability region. Larger C improves stability.

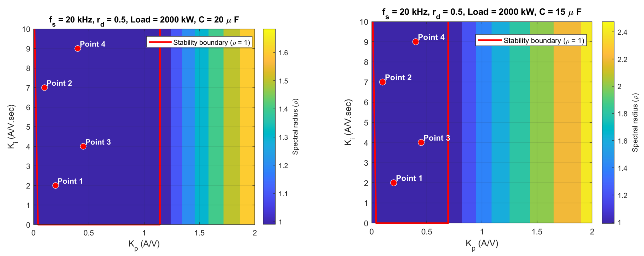

(a) $C = 20\mu F, f_s = 20kHz$ (b) $C = 15\mu F, f_s = 20kHz$

Fig. 10. Increased sampling frequency enables larger stability region with lower terminal capacitance.

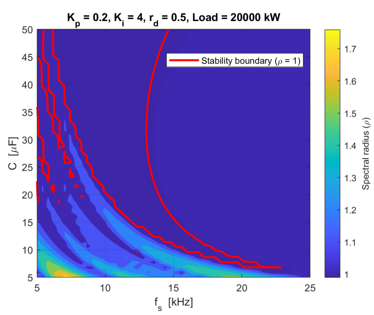

Fig. 11. Stability map of the five-converter system in terms of C and f_s.

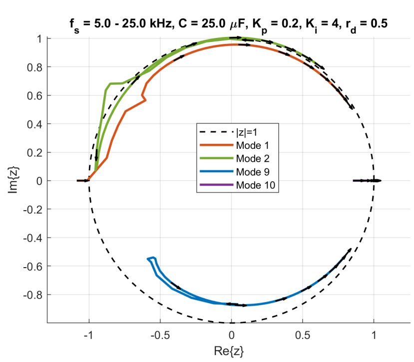

Fig. 12. Modes of the closed loop system as frequency changes.

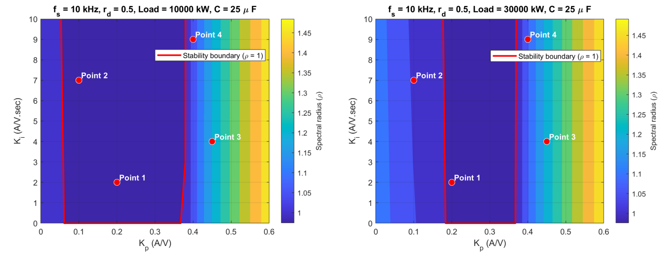

(a) Load = 10 MW (b) Load = 30 MW

Fig. 13. Effect of load variation on stability region. Higher loads shrink the stable region.

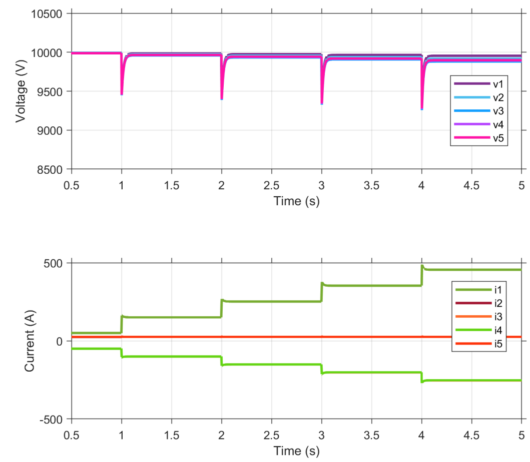

Fig. 14. Time domain simulation results for a load change from 2 MW to 5 MW with robust selection of controller parameters.

References

[1] International Electrotechnical Commission, "Medium voltage DC (MVDC) grids for an all-electric society," International Electrotechnical Commission (IEC), Geneva, Switzerland, Tech. Rep., Sep. 2025.

[2] S. Coffey, V. Timmers, R. Li, G. Wu, and A. Egea-Àlvarez, "Review of MVDC Applications, Technologies, and Future Prospects," *Energies*, vol. 14, no. 24, p. 8294, Dec. 2021.

[3] M. Su, Z. Liu, Y. Sun, H. Han, and X. Hou, "Stability Analysis and Stabilization Methods of DC Microgrid With Multiple Parallel-Connected DC–DC Converters Loaded by CPLs," *IEEE Transactions on Smart Grid*, vol. 9, no. 1, pp. 132–142, Jan. 2018.

[4] Y. Huangfu, S. Pang, B. Nahid-Mobarakeh, L. Guo, A. K. Rathore, and F. Gao, "Stability Analysis and Active Stabilization of On-board DC Power Converter System with Input Filter," *IEEE Transactions on Industrial Electronics*, vol. 65, no. 1, pp. 790–799, Jan. 2018.

[5] S. Pang, B. Nahid-Mobarakeh, S. Pierfederici, Y. Huangfu, G. Luo, and F. Gao, "Large-Signal Stable Nonlinear Control of DC/DC Power Converter With Online Estimation of Uncertainties," *IEEE Journal of Emerging and Selected Topics in Power Electronics*, vol. 9, no. 6, pp. 7355–7368, Dec. 2021.

[6] S. Anand and B. G. Fernandes, "Reduced-Order Model and Stability Analysis of Low-Voltage DC Microgrid," *IEEE Transactions on Industrial Electronics*, vol. 60, no. 11, pp. 5040–5049, Nov. 2013.

[7] A. Navarro-Rodríguez, P. García, J. M. Cano, and M. Sumner, "Dynamic Analysis, Stability and Design of Grid Forming Converters With PI-Based Voltage Control in DC and 3-Phase AC Micrgrids," *IEEE Transactions on Energy Conversion*, vol. 38, no. 4, pp. 2249–2262, Dec. 2023.

[8] Y. Gui, R. Han, J. M. Guerrero, J. C. Vasquez, B. Wei, and W. Kim, "Large-Signal Stability Improvement of DC-DC Converters in DC Microgrid," *IEEE Transactions on Energy Conversion*, vol. 36, no. 3, pp. 2534–2544, Sep. 2021.

[9] D. Niu, Z. Wang, M. Chen, and J. Fang, "On Transient Stability Problems in DC Microgrids," *Applied Sciences*, vol. 14, no. 24, p. 11523, Dec. 2024.